FINITE ELEMENT PREDICTION OF RESIN POCKET GEOMETRIES AROUND OPTICAL FIBERS EMBEDDED IN LAMINATED COMPOSITES

N.Lammens[a*], G. Chiesura[a], E. Voet[a], G. Luyckx[a], W. Van Paepegem[a], J. Degrieck[a] A.

[a]*Department of Materials Science & Engineering, UGent, Technologiepark-Zwijnaarde 903, 9052 Zwijnaarde, BELGIUM*
**Nicolas.Lammens@ugent.be*

Keywords: optical fiber sensors, composites, finite element, resin pocket.

Abstract
This work presents a finite element technique allowing the accurate prediction of resin pocket geometries in laminated composites. The F.E. implementation relies solely on material models and element formulations readily available in all commercial F.E. codes. Only a minimal amount of material characterization is required using straightforward testing equipment. The F.E. results are validated with microscopic images of several different lay-up laminates with embedded optical fibers of different diameters. Very good correspondence is found between F.E. results and microscopic cross-sections.

1. Introduction

With the increasing use of composite materials, much research is being performed into the concept of 'smart structures'. Equipped with a multitude of sensors, these structures are capable of responding to certain inputs ranging from the more basic stress/strain sensing, to more advanced features such as morphing geometries and structural health monitoring. The EU FP7 'SmartFiber' project even aims at embedding both sensor and read-out equipment inside the composite host, providing a fully embedded health-monitoring system. By embedding the sensor and read-out system during production of the part, these parts are protected from environmental factors while at the same time providing the additional capability of monitoring the production cycle.

Due to the fibrous nature of composite structures, the presence of any foreign structure will distort the surrounding material properties and impact the performance of the final part [1-9]. These distortions will impact both the accuracy of the sensor as well as the fatigue behavior of the structure, and must therefore be analyzed and reduced if possible. When optical fiber sensors are embedded in laminated composites, a characteristic lenticular 'resin pocket' occurs surrounding the optical fiber sensor.

Dasgupta et al [10] presented an analytical framework to determine the resin pocket geometry based on easily accessible material properties such as reinforcing fiber stiffness and diameter. Employing the Rayleigh-Ritz variational method, Dasgupta approximated the resin pocket geometry by a series of beam functions. While good correspondence with microscopic images was achieved, the convergence of the algorithm proved very difficult and time consuming.

Case et al [11] modified the energy formulation presented by Dasgupta and used a sinusoidal displacement field rather than a series of beam functions. Although this displacement function violates the assumptions of classical beam theory, the resulting simplifications allowed the author to extract an analytical expression for the resin pocket geometry. Her et al [12] used a sinusoidal displacement field similar to that of Case. Additionally, Her consider that the resin pocket is not necessarily symmetric through the thickness of the laminate, and modified the formulation given by Dasgupta to account for this effect.

These implementations resulted in good correspondence with experimental samples produced using a caul-plate generating a flat top and bottom surface. In the absence of a caul-plate however, the required displacement functions are more difficult to define. Additionally, the methods discussed are only applicable to simple geometries such as optical fibers with infinite length. More general inclusions or 3D inclusions cannot be modeled using this approach since the required displacement fields are unknown for these circumstances.

This work will present an alternative method to the determination of resin pocket geometry, based on F.E. formulations. Although much research has been performed into the large-scale drape behavior of composites, these methods often use proprietary codes and material models, which require extensive material characterization. The proposed approach differs from these drape simulations by relying solely on standard elements, material models and F.E. formulations. Additionally, for the simulation of UD materials, the required material characterization is limited to very basic tests. Compared to the analytical method proposed by Dasgupta, the proposed model is more flexible as it allows the user to simulate any form of inclusion.

2. Experimental samples

2.1. Microscopic samples

In order to evaluate the accuracy of the F.E. model, different samples were created. All samples were made out of carbon fiber reinforced epoxy (M18 matrix reinforced with M55J carbon fiber, by Hexcel), and cured in a vacuum bag with an autoclave cycle of 2 hours at 180°C (with a ramp of 3°C/min and a 20 min. soak at 120°C) at 7 bar of nitrogen pressure. Different diameter optical fiber sensors were embedded. The fibers were Ormocer coated draw-tower fibers. Table 1 describes the different samples created for this work

Specimen name	Stacking sequence	Number of samples
UD-90-1	90_2/**OF-125**/90_2	3
UD-90-2	90_4/**OF-125**/90_4	3
UD-90-3	90_8/**OF-125**/90_8	3
UD-45-1	45_2/**OF-60**/45_2	3
UD-45-2	45_2/**OF-80**/45_2	1
UD-45-3	45_2/**OF-125**/45_2	3
CP-1	$0_2/90_2/0_2/90_2$/**OF-60**/$90_2/0_2/90_2/0_2$	3
CP-2	$0_2/90_2/0_2/90_2$/**OF-80**/$90_2/0_2/90_2/0_2$	3
CP-3	$0_2/90_2/0_2/90_2$/**OF-125**/$90_2/0_2/90_2/0_2$	3

OF-60: 60µm fiber, 106µm coating, **OF-80:** 80µm fiber, 129µm coating, **OF-125:** 125µm fiber, 200µm coating

Table 1. Detail of sample lay-up

After curing, the samples are cut perpendicular to the OF using a diamond blade and polished. The final samples are examined under an optical microscope with calibrated magnifications allowing us to measure distances on the images (Figure 1).

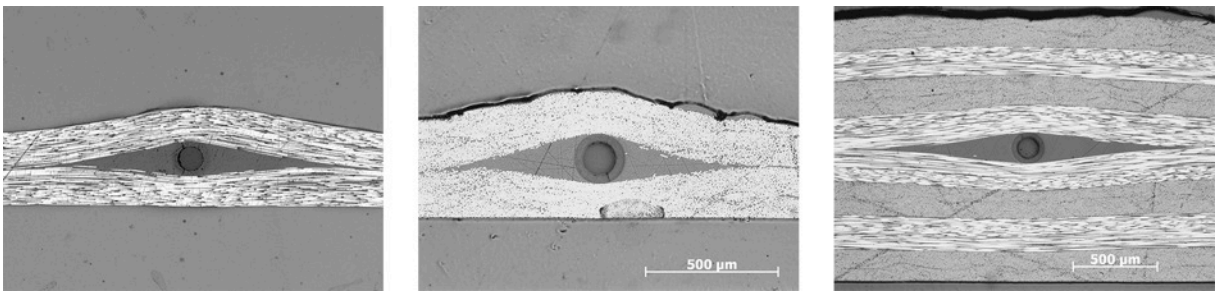

Figure 1. Microscopic images of carbon fiber reinforced laminates with embedded optical fibers (left-to-right: UD-90-1, UD-45-3, CP-3)

2.2. Bending samples

Due to sliding between the reinforcing fibers, bending stiffness of an uncured composite laminate cannot be calculated based on in-plane properties and geometry. Several methods can be employed to measure the bending stiffness of fabric or fibrous materials such as the Pierce cantilever test, heart loop test or Kawabata KES. However, these test methods were designed with dry fabrics in mind, and are not easily adapted to test prepreg material at elevated temperatures. In order to estimate the bending stiffness of the prepreg material used, without the need for expensive test equipment, a simple cantilever test was performed in which a single ply heated (to 180°C, the curing temperature specified for this material) and allowed to bend under the influence of gravity. Different lengths of prepreg were tested. After curing, the vertical displacement was measured. The determined displacements are gathered in Table 2. Note that due to the large displacements, beam theory is no longer valid for these experiments.

Sample length	Vertical displacement
50mm	7mm
70mm	21mm
90mm	45mm
110mm	76mm
130mm	120mm
150mm	140mm

Table 2. Vertical displacements for various lengths of cantilevered specimens

3. Material parameters

The aim of this work is to be able to predict the resin pocket geometry by using only standard material models and element types available in commercial F.E. packages. Many different approaches can be found in literature on how to model the curing of a reinforced epoxy. A very common approach leading to accurate cure simulations is to use a so-called ‘cure hardening instantaneously linear elastic’ (CHILE) model in which the assumption is made that at every point in time the laminate responds in a linear elastic way, but with an elasticity that evolves through time. It has been shown that a properly calibrated CHILE model produces equivalent results as visco-elastic modeling, at only a fraction of the computational cost. Considering that the forming of the resin pocket will take place in the early stages of the

curing process (when viscosity is low), the CHILE model can be reduced to a purely elastic material model. Additionally, due to the fact that we are using unidirectional (UD) prepreg material, the material model should exhibit transverse isotropic behavior. Consequently, we will use a linear elastic orthotropic material model.

Researchers have shown that composite forming is dominated by (i) intra-ply shearing, (ii) intra-ply tensile loading, (iii) ply/ply and ply/tool shearing, (iv) ply bending and (v) compaction/consolidation.

3.1. Intra-ply shearing

In the case of UD material, intra-ply shearing is exclusively due to shearing of the epoxy matrix. Furthermore, if the 1-direction is oriented along the reinforcements, transverse isotropy demands that $G_{12} = G_{13}$. With the 2-direction in-plane and perpendicular to the reinforcements, we expect the 1-direction to be the stiffest direction in the plane of the ply, while the 2-direction represents the weakest direction. This restricts the range of allowable values for G_{12}, based on the exact values of E_{11}, E_{22} and the in-plane Poisson coefficient ν_{12}. Given the values stated in Table 3, G_{12} must be between 20MPa and 100GPa. It was found that a value of $G_{12} = G_{13} = 300$MPa led to the best correspondence between F.E. and experiments. Note that this value is still significantly larger than those found in literature. However, the modifications to the model necessary to achieve the correct bending behavior (discussed later), severely reduce the macroscopic shear behavior of a single ply.

3.2. Intra-ply tensile loading

The F.E. model should have the correct response to intra-ply tensile loading. We assume that when the resin pocket is formed, the low-viscosity epoxy has a negligible load-bearing capacity. Based on this assumption, the tensile modulus in the reinforcement direction is determined solely by the carbon fiber stiffness and fiber volume fraction. The axial tensile modulus for M55J is stated to be 540GPa. The volume fraction of the uncured prepreg is 55,21%. This leads to an in-plane stiffness along the reinforcement direction of $E_{11} = 298$GPa. This stiffness in the 2-direction (in-plane, perpendicular to the reinforcements) should be equal to the stiffness in the 3-direction due to transverse isotropy assumptions. This value is determined later.

3.3. Ply/ply shearing

In general ply/ply shearing is both pressure and rate dependent. However, the tests to determine these dependencies require specialized equipment beyond the aims of this work. We will assume a constant coefficient of friction equal to 0.14, which is a general value for lubricated carbon-carbon friction. Note that this does not limit the usability of the model. Most F.E. software allows for pressure-dependent contact formulations, allowing the modeling of pressure dependency if required.

3.4. Ply bending

Bending stiffness of plies is much lower than what would be found using beam theory. Compared to the values stated in Table 2, using an in-plane stiffness of $E_{11} = 298$GPa and a ply thickness of 105µm, beam theory would only predict a deflection of 45µm for a beam of 50mm length. Overcoming this issue is critical for this work. In most drape modeling

research, the bending stiffness is either completely ignored by using membrane elements, or specialized user elements are written which decouple bending and in-plane behavior. While ignoring bending stiffness is acceptable in certain large-scale experiments, it cannot be ignored in the forming of resin pockets. Additionally, using membrane elements would prohibit modeling of through-thickness compaction, which is discussed next. On the other hand, implementing and validating a user element is very time consuming and is usually detrimental to the performance of F.E. algorithms.

In order to decouple bending behavior from in-plane properties, we model a single ply of prepreg material by a number of layers, tied together by friction. Using beam theory as a starting point, we find that we need 12 layers per ply in order to achieve comparable bending behavior as found through experiments. The friction coefficient between layers is chosen equal to the ply/ply shearing coefficient. In order to compare the bending behavior with experimental data, a 12-layered ply is modeled in ABAQUS and a cantilever test is simulated. Figure 2 shows the vertical displacements predicted by F.E. compared to the values measured in experiments.

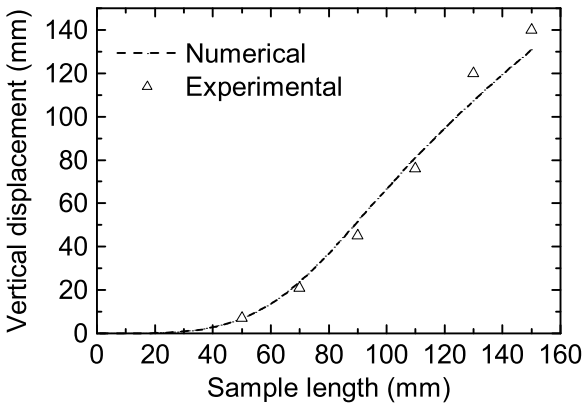

Figure 2. F.E. simulation of cantilever bending experiments

Good correspondence between F.E. and experiment is found. Note that for longer lengths (> 90mm) a slightly smaller displacement is predicted than found in experiments. This can be attributed partly to the fact that the F.E. model is only an approximation of a real cure cycle. On the other hand, during curing, epoxy will probably droop to the lowest point, creating additional tip-loads on the beam. This effect will be more pronounced for longer beams and is not captured in the F.E. model. Considering that the forming simulations of interest in this work will never contain such large deformations, we can conclude that this modeling approach is sufficiently accurate for our goals.

3.5. Compaction

During the curing process, epoxy is extracted from the prepreg into the breather/bleeder material under the influence of external pressure, leading to a thinner part and higher volume fraction. Several authors have proposed a simple relationship between volume fraction and curing pressure:

$$V_f = V_{f0} \cdot P^B \quad (1)$$

where B is an empirical factor called the stiffening index, V_{f0} the initial volume fraction and V_f the final volume fraction.

Based on measured cured-ply-thickness (CPT) values of samples UD-90-x an average CPT of 95µm was found with a standard deviation of 2µm, which equates to a cured fiber volume fraction of 61.06%. Having been achieved under a pressure of 8 bar (7 bar nitrogen + 1 bar vacuum), this results in a linear through-thickness stiffness of $E_{33} = E_{22} = 8.4$MPa. However, considering $V_f \sim 1/t$, where t represents the ply thickness, Equation (1) reveals that we cannot capture the precise compaction response with a linear elastic material model. Initial F.E. simulations with $E_{33} = E_{22} = 8.4$MPa showed an overestimation in compression beneath the optical fiber. Slightly modifying the stiffness revealed $E_{33} = E_{22} = 13.5$MPa to produce more accurate results. In order for the global response of the ply to remain correct (i.e. compress to 95µm under 8 bar of pressure), the initial thickness of the ply has to be reduced to 101µm.

Finally, a distinction must be made between plies above the optical fiber and those below. As a first assumption, the bottom layers must behave according to the compaction behavior described previously. However, the top layers will respond differently since in reality epoxy in these layers can flow out towards the breather/bleeder material or into the resin pocket. This behavior cannot be modeled by the F.E. implementation and would result in incorrect deformations. In order to resolve this issue, we model the top layers as if all excess epoxy was already removed prior to the simulation. As a result, the top layers have a layer thickness equal to the CPT (95µm) and an increased transverse stiffness.

3.6. Poisson coefficient

During the first stages of curing, the epoxy can be thought of as being a liquid and therefore incompressible. Using the orthotropic material properties derived previously, incompressibility would require $\nu_{12} = \nu_{13} = 0.5$ and $\nu_{23} = 0.99$. However, this does not account for the ability of the resin to fill the resin pocket or being extracted into the breather/bleeder material. Therefore, the strict incompressibility needs to be reduced in the 2-3-plane. For simplicity, $\nu_{12} = \nu_{13} = \nu_{23} = 0.5$ is chosen as a starting point for the material model.

The optical fiber is modeled as an isotropic material (E = 72.9 GPa, ν = 0.17). The Ormocer coating is modeled as an isotropic material (E = 200MPa, ν = 0.32) where the stiffness was reduced due to the increased temperature. The initial ply material parameters are gathered in Table 3.

	Young's modulus	**Poisson ratio**	**Shear modulus**
M18/M55J	E_{11} = 298 GPa	ν=0.5	G_{12} = 300 MPa
(bottom layers - 101 µm)	E_{22} = 13.5 MPa		G_{13} = 300 MPa
	E_{33} = 13.5 MPa		G_{23} = 4.5 MPa
M18/M55J	E_{11} = 298 GPa	ν=0.5	G_{12} = 300 MPa
(top layers - 95 µm)	E_{22} = 40 MPa		G_{13} = 300 MPa
	E_{33} = 40 MPa		G_{23} = 13 MPa

Table 3. Initial material parameters

4. F.E. model

All simulations were performed in ABAQUS/standard. Exploiting the periodicity of the model in the optical fiber direction, a generalized plane strain model was used to decrease

computational times. Additionally symmetry around the optical fiber was used to only model half of the laminate. The tooling was modeled as a frictionless support. A biased mesh was used for the plies, decreasing element size towards the inclusion. A single ply was modeled using 7140 CPEG4 elements. The optical fiber was meshed using 702 CPEG4 and 78 CPEG3 elements. A mesh convergence study was performed with a refined mesh using 45960 CPEG4 elements per ply. No appreciable differences were noticeable in the deformed shape.

A load of 8 bar was applied on the top surface of the laminate and gravitational load was applied to the entire model. Friction was defined between all layers with a friction coefficient of 0.14. The contact between the optical fiber and laminate was modeled to be frictionless.

The deformed coordinates of each ply were exported and processed in MATLAB to compare the F.E. results to microscopic images. The calibrated scale from the microscopic images was used to overlay the F.E. coordinates on the microscopic images. The results of the different F.E. simulations are shown in Figure 3.

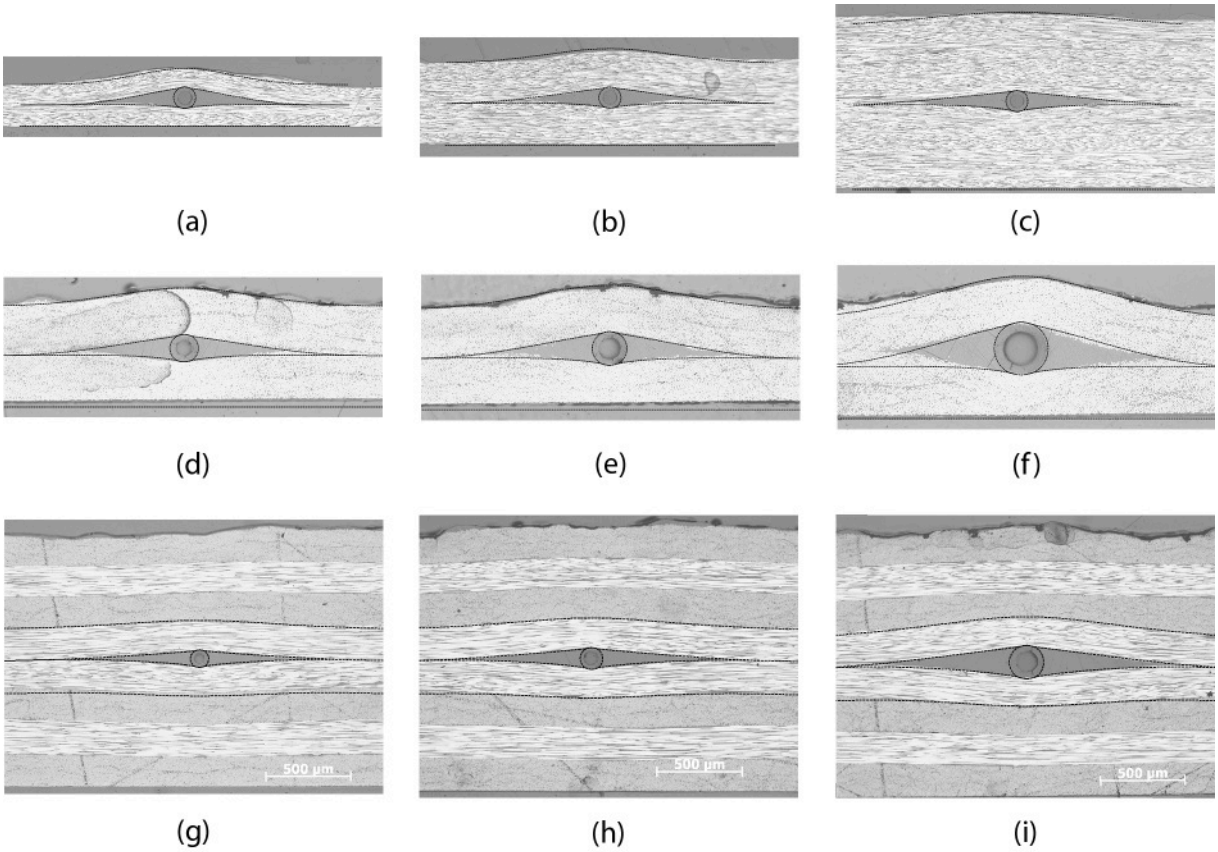

Figure 3. Resin pocket and F.E. predictions (dotted lines): (a) UD-90-1, (b) UD-90-2, (c) UD-90-3, (d) UD-45-1, (e) UD-45-2, (f) UD-45-3, (g) CP-1, (h) CP-2, (i) CP-3

5. Conclusions

In this work, a finite element method was presented allowing modeling of the resin pocket geometry surrounding optical fiber sensors using a limited amount of experimental material characterization and standard material models and finite element formulations. The results shown in Figure 3 clearly illustrate the very good correspondence between experimental results and finite element predictions. The approach was illustrated on different inclusions

sizes, laminate thicknesses and stacking orientations showing the general validity of the method. Future work will evaluate the usability of the method on larger inclusions.

Acknowledgements

The research leading to these results has received funding from the European Union Seventh Framework Programme FP7/2007-2013 under grant agreement n° 257733 (SmartFiber)

References

[1] B. Benchekchou and N. S. Ferguson, "The effect of embedded optical fibres on the fatigue behaviour of composite plates," *Composite Structures,* vol. 41, pp. 113-120, Feb 1998.

[2] C. Choi, D. C. Seo, J. J. Lee, and J. K. Kim, "Effect of embedded optical fibers on the interlaminar fracture toughness of composite laminates," *Composite Interfaces,* vol. 5, pp. 225-240, 1998.

[3] R. Hadzic, S. John, and I. Herszberg, "Structural integrity analysis of embedded optical fibres in composite structures," *Composite Structures,* vol. 47, pp. 759-765, Dec 1999.

[4] D. C. Lee, J. J. Lee, and S. J. Yun, "The Mechanical Characteristics of Smart Composite Structures with Embedded Optical-Fiber Sensors," *Composite Structures,* vol. 32, pp. 39-50, 1995.

[5] H. Y. Ling, K. T. Lau, and C. K. Lam, "Effects of embedded optical fibre on mode II fracture behaviours of woven composite laminates," *Composites Part B-Engineering,* vol. 36, pp. 534-543, 2005.

[6] L. G. Melin, K. Levin, S. Nilsson, S. J. P. Palmer, and P. Rae, "A study of the displacement field around embedded fibre optic sensors," *Composites Part a-Applied Science and Manufacturing,* vol. 30, pp. 1267-1275, 1999.

[7] D. C. Seo and J. J. Lee, "Effect of Embedded Optical-Fiber Sensors on Transverse Crack Spacing of Smart Composite Structures," *Composite Structures,* vol. 32, pp. 51-58, 1995.

[8] K. Shivakumar and L. Emmanwori, "Mechanics of failure of composite laminates with an embedded fiber optic sensor," *Journal of Composite Materials,* vol. 38, pp. 669-680, 2004.

[9] M. Surgeon and M. Wevers, "Static and dynamic testing of a quasi-isotropic composite with embedded optical fibres," *Composites Part a-Applied Science and Manufacturing,* vol. 30, pp. 317-324, 1999.

[10] A. Dasgupta, Y. Wan, and J. S. Sirkis, "Prediction of resin pocket geometry for stress analysis of optical fibers embedded in laminated composites," *Smart Materials and Structures,* vol. 1, p. 101, 1992.

[11] S. W. Case and G. P. Carman, "Compression Strength of Composites Containing Embedded Sensors or Actuators," *Journal of Intelligent Material Systems and Structures,* vol. 5, pp. 4-11, Jan 1994.

[12] S. C. Her, B. R. Yao, S. C. Lan, and C. Y. Liu, "Stress Analysis of a Resin Pocket Embedded in Laminated Composites for an Optical Fiber Sensor," in *Advanced Design and Manufacture Ii*. vol. 419-420, D. Su, Q. B. Zhang, and S. F. Zhu, Eds., ed, 2010, pp. 293-296.